Version of Record: https://www.sciencedirect.com/science/article/pii/S0039602824002164
Manuscript_169d0b7c236fd775574a24d1fec58eca

CO–induced roughening of Cu(111): formation and detection of reactive nanoclusters on metal surfaces

Konstantinos G. Papanikolaou, Lang Xu, Evangelos Smith, and Manos Mavrikakis†

Department of Chemical and Biological Engineering, University of Wisconsin–Madison, 1415 Engineering Drive, Madison, WI 53706, United States

ORCID's:

(1) Konstantinos G. Papanikolaou: 0000-0002-5948-7955

(2) Lang Xu: 0000-0001-5959-8797

(3) Evangelos Smith: 0000-0001-6926-2306

(4) Manos Mavrikakis: 0000-0002-5293-5356

Graphical Abstract

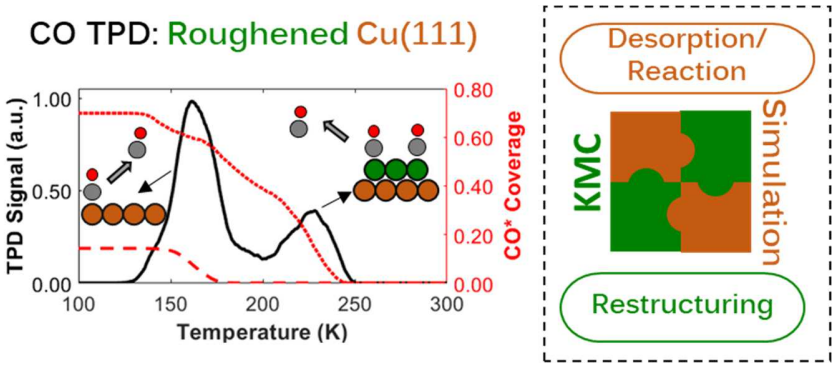

Highlights:

- Distinct reactivity of Cu nanoclusters compared to Cu(111)
- Kinetic Monte Carlo simulation combining surface reaction and surface restructuring
- Ejection of copper atoms from step edges driven by adsorbed surface species
- Temperature Programmed Desorption of CO for the detection of nanoclusters on metal surfaces

Keywords: catalyst dynamic restructuring; reactive metal nanoclusters; coverage effects; density functional theory; temperature programmed desorption; kinetic Monte Carlo.

Abstract

The formation of nanoclusters on metal surfaces in the presence of reactive environments is a phenomenon with important implications for catalysis. These nanoclusters are composed of atoms ejected from undercoordinated sites such as step edges, and their presence alters the catalytic properties of solid materials. We perform density functional theory (DFT) and kinetic Monte Carlo (KMC) simulations to investigate the formation and reactivity of copper clusters on Cu(111). Our results indicate a considerably higher reactivity of small copper nanoclusters, with up to seven atoms in size on roughened copper surfaces than on pristine Cu(111) and Cu(211). Regarding the restructuring events that give rise to nanoclusters under CO atmospheres, we determine that the ejection of Cu atoms from step edges and their migration therefrom to adjacent Cu(111) terraces are, by and large, driven by CO coverage effects. By means of KMC simulations, which account for CO–CO lateral interactions and CO–induced surface restructuring, we show that temperature programmed desorption (TPD) holds promise for the detection of highly reactive nanoclusters. Our approach showcases how surface restructuring and surface–adsorbate bond breaking can be combined when modeling surface reactions and contributes to the development of an advanced understanding of the nature of active site under reaction conditions.

1. Introduction

The dynamic restructuring of catalytic surfaces during reaction has a great impact upon their performance [1,2]. Pure metal and alloy surfaces undergo structural changes under vacuum conditions (e.g., quasi–hexagonal reconstruction of Pt(100); (1 x 2) missing row reconstruction of Pt(110)) [3,4], or more often in the presence of strongly bound species (e.g., CO, NO, O, H etc.) [5–15]. In this regard, CO is a particularly interesting adsorbate because: (1) it is ubiquitous in catalytic reactions either as a reactant, intermediate, or as an impurity; (2) it interacts strongly with most transition metal surfaces and can alter their microscopic structure and morphology; and (3) it is commonly used to probe the structure of single crystals and supported catalysts [16].

High–pressure scanning tunneling microscopy (HP–STM) studies have brought into light a noteworthy type of surface restructuring, whereby metal surfaces break up into reactive two–dimensional nanoclusters when exposed to CO [17,18]. This phenomenon is known as *surface roughening* and is promoted by the strong interaction between adsorbates and undercoordinated sites exposed in nanoclusters, thereby minimizing the chemical potential of the adsorbate/substrate system [19]. One factor characterizing the tendency of a metal surface to undergo such a structural change is provided by the cohesive energy of the metal [20]. Surface science has shown that surfaces of "soft" metals like Cu and Au (cohesive energies of 3.49 eV and 3.81 eV, respectively [20]) decompose into nanoclusters upon exposure to CO [19,21,22], whereas the close–packed Rh(111) and Pt(111) surfaces (cohesive energies of 5.75 eV and 5.84 eV for Rh and Pt, respectively) remain atomically flat upon similar exposures to CO [17,23].

The roughening of Cu surfaces is important because Cu–based materials are commonly used to catalyze chemical reactions of practical and scientific interest (e.g., water–gas shift reaction,

methanol synthesis, catalytic CO oxidation etc.) [24–28]. This phenomenon has been observed on several Cu low–index surfaces. Cu(111) was studied by means of HP–STM revealing that at CO pressures larger than 0.10 Torr and 298 K the terraces of the single crystal became covered by triangular (ca. 3 Cu atoms – Cu_3) and hexagonal (ca. 19 Cu atoms – Cu_{19}) nanoclusters [19]. The latter were stable after the evacuation of CO gas and capable of dissociating H_2O [19], a molecule that is not activated on pristine Cu(111) because of the weak H_2O–Cu(111) interaction [29]. The formation of Cu nanoclusters over Cu(111) was later confirmed by our previous *ab initio* kinetic Monte Carlo (KMC) simulations in ref. [30], where we demonstrated that surface roughening is a broader phenomenon relevant to catalysis by metals [31]. Earlier work determined that Cu(100) subjects to roughening when exposed to CO gas [32]. At room temperature, a CO pressure of ca. 0.20 Torr was sufficient to form rectangular Cu_5 nanoclusters on Cu(100) [32]. The presence and thermodynamic stability of Cu_5 was corroborated by X–ray photoelectron spectroscopy (XPS), temperature–programmed desorption (TPD) and density function theory (DFT) [33,34]. These studies concluded that the roughened Cu(100) crystal could perform the cleavage of the C–O bond in CO, namely a bond scission that is kinetically limited over pristine surfaces of coinage metals (e.g., activation barrier of 3.84 eV on Cu(111) [35]). CO_2 is another species that brings about the roughening of Cu(100) by first dissociating to CO in step edges followed by CO–induced ejection of Cu atoms therefrom [36]. Finally, in the presence of CO, Cu(110) decomposed into linearly–arranged nanoclusters that [19], similar to the hexagonal Cu clusters on Cu(111), were active toward H_2O activation [37].

These studies demonstrate that the formation of nanoclusters may convert relatively inert surfaces into highly active surfaces for catalysis. Importantly, this phenomenon is relevant to supported catalysts given their exposure to extreme conditions during reaction and calcination

(i.e., high temperatures and pressures). In this work, we present a first–principles–based modeling approach capable of predicting if a surface is susceptible to breaking up into nanoclusters and the conditions where this may occur. We decipher restructuring events that take place during roughening and eventually lead to the formation of nanoclusters on Cu(111) under vacuum and CO environments. We show that the ejection of Cu atoms from the step edge of Cu(211) and their migration to (111) terraces are heavily dependent on CO coverage. Furthermore, by means of KMC simulations, we model TPD spectra for the desorption of CO from the pristine Cu(111), Cu(211) surfaces and Cu(111) roughened by nanoclusters. Our KMC results suggest that TPD, a common technique in experimental surface science, could be employed for the detection of nanoclusters. Overall, we find that our results are in good agreement with experimental findings. The presented approach contributes to the development of accurate theoretical models for the prediction of surface roughening and to the development of computational models that go beyond the traditional assumption of static surfaces during reaction.

2. Computational details

Density Functional Theory: Planewave DFT was used to calculate energetics using the Vienna Ab initio Simulation package (VASP) [38,39]. Core electronic states were described with the projector–augmented wave (PAW) method [40]. Several methods have been demonstrated to address the site preference error of DFT for CO adsorption on extended metal surfaces, including: (1) on-site U corrections [41]; (2) relativistic corrections [42]; (3) corrections to the CO singlet-triplet splitting excitation energy [43]; and (4) use of hybrid functionals [44]. In this study, we treat exchange and correlation using the PBE+U method with U = 6.0 eV for C and O

atoms [41,45]. This method increases the gap between the highest occupied molecular orbital and the lowest unoccupied molecular orbital (i.e., HOMO–LUMO gap) of CO by shifting the CO $2\pi^*$ orbital to higher energy and provides accurate results for the CO/Cu(111) system [46]: it correctly predicts the most stable adsorption site (i.e., CO perpendicularly adsorbed on a top site) and the experimentally determined binding energy of CO on a top site of Cu(111) (i.e., 0.49 ± 0.015 eV) at low surface coverage [19,47,48]. We computed a Cu lattice constant of 3.63 Å, which is in good agreement with experiment (3.59 ± 0.004 Å) [49]. Step edges of the Cu(111) crystal were modeled with a Cu(211) surface that contains a step edge connected with a lower and an upper terrace (see Figure S1). The Cu(111) and Cu(211) surfaces were modeled by four–layer (4 × 4) and (4 × 1) slabs, respectively. In both cases, the bottom two layers were kept fixed during geometry optimization, while the top two layers and any adsorbates were allowed to relax. The kinetic energy cut–off for the planewave basis was 400 eV. The first Brillouin zone of Cu(111) and Cu(211) slabs were sampled with a 3 × 3 × 1 and a 5 × 4 × 1 Monkhorst–Pack k–mesh [50], respectively. Electronic self–consistency was assured up to a tolerance 10^{-5} eV, and all ionic relaxations were converged to a force tolerance of 0.02 eV/Å.

The adsorption energy of an adsorbate species A* (* indicates an adsorbed species) on Cu(111) and Cu(211) was calculated as $\Delta E_{ads}(A*) = E_{DFT}^{A*+slab} - E_{DFT}^{slab} - E_{DFT}^{A_{(g)}}$, where $E_{DFT}^{A*+slab}$ is the total energy of the slab with A* adsorbed thereon, E_{DFT}^{slab} is the total energy of the clean slab, and $E_{DFT}^{A_{(g)}}$ is the total energy of A species in the gas phase. Based on this definition, more negative $\Delta E_{ads}(A*)$ indicates stronger interaction with the surface. The reported CO differential adsorption energies were computed as $\Delta E_{diff}(CO*) = E_{DFT}^{N\times CO*} - E_{DFT}^{(N-1)\times CO*} - E_{DFT}^{CO_{(g)}}$, where $E_{DFT}^{N\times CO*}$ and $E_{DFT}^{(N-1)\times CO*}$ are the total energies of slabs with N × CO* and (N – 1) × CO*

molecules adsorbed, respectively, and $\mathrm{E}_{\mathrm{DFT}}^{\mathrm{CO(g)}}$ is the total energy of CO in the gas phase. $\Delta\mathrm{E}_{\mathrm{diff}}(\mathrm{CO}*) < 0$ implies that N^{th} CO prefers to adsorb on the surface with (N – 1) CO molecules already adsorbed thereon, than to remain in the gas phase, while the opposite is true for $\Delta\mathrm{E}_{\mathrm{diff}}(\mathrm{CO}*) > 0$. Transition states (TSs) for Cu atom ejection events were located using a combination of the climbing image nudged elastic band (CI-NEB) method, the dimer method, and quasi–Newton optimization [51,52]. Vibrational frequency analyses with a displacement of 0.02 Å verified the identity of TSs, which had only one vibrational frequency that corresponded to motion along the reaction coordinate. The activation energy barrier for specific elementary steps were defined as $\mathrm{E_a} = \mathrm{E_{TS}} - \mathrm{E_{IS}}$, where $\mathrm{E_{TS}}$ and $\mathrm{E_{IS}}$ are the total energies of the TS and initial state (IS), respectively. Reaction energies were defined as $\Delta\mathrm{E_{rxn}} = \mathrm{E_{FS}} - \mathrm{E_{IS}}$, where $\mathrm{E_{FS}}$ is the total energy of the final state (FS). Surface coverages were defined as the number of adsorbates divided by the number of atoms in the top layer. Fractional CO* coverages for Cu* nanoclusters were defined as the number of CO* species adsorbed on a nanocluster divided by the number of Cu* atoms in the nanocluster (eq. (S10) and (S11) in the Supplementary Material).

Finally, we assessed the enthalpic preference for Cu ejected atoms from the step edge of Cu(211) to remain in the vicinity of the step edge as adatoms versus to migrate to the main terrace of Cu(111) and aggregate with a preexisting cluster/adatom thereon. Accordingly, we defined cluster formation energies. Under vacuum conditions, the cluster formation energy is

$$\Delta E_{cluster,f}^{Vac} = \left\{E_{211}^{(m-1)\,\mathrm{x}\,Cu*} + E_{111}^{k\,\mathrm{x}\,Cu*}\right\} - \left\{E_{211}^{m\,\mathrm{x}\,Cu*} + E_{111}^{(k-1)\,\mathrm{x}\,Cu*}\right\}, \quad (1)$$

where $E_{211}^{(m-1)\,\mathrm{x}\,Cu*}$ ($E_{211}^{m\,\mathrm{x}\,Cu*}$) is the total energy of a Cu(211) slab with $m-1$ (m) Cu* adatoms next to the step edge (see panel (A) in Figure S7); $E_{111}^{k\,\mathrm{x}\,Cu*}$ ($E_{111}^{(k-1)\,\mathrm{x}\,Cu*}$) is the total energy of a Cu(111) slab with a copper nanocluster consisting of k ($k-1$) Cu* adatoms. $\Delta E_{cluster,f}^{Vac} > 0$ indicates a thermodynamic preference for the ejected adatom to remain adsorbed next to the step

edge, while $\Delta E^{Vac}_{cluster,f} < 0$ indicates a thermodynamic preference for the adatom to aggregate with a pre–existing cluster of $k-1$ atoms on the Cu(111) terrace and form a cluster of k Cu adatoms. Along the same lines, the cluster formation energy in the presence of adsorbed CO* is:

$$\Delta E^{CO*}_{cluster,f} = \left\{E^{(m-1)\,x\,Cu* + (n-1)\,x\,CO*}_{211} + E^{k\,x\,Cu* + f\,x\,CO*}_{111}\right\} - \left\{E^{m\,x\,Cu* + n\,x\,CO*}_{211} + E^{(k-1)x\,Cu* + (f-1)x\,CO*}_{111}\right\}, \quad (2)$$

where $E^{(m-1)\,x\,Cu* + (n-1)\,x\,CO*}_{211}$ ($E^{m\,x\,Cu* + n\,x\,CO*}_{211}$) is the total energy of a Cu(211) slab with $m-1$ (m) Cu* next to the step edge (see panel (B) in Figure S7) and $n-1$ (n) CO* adsorbates; $E^{k\,x\,Cu* + f\,x\,CO*}_{111}$ ($E^{(k-1)x\,Cu* + (f-1)x\,CO*}_{111}$) is the total energy of a Cu(111) slab with k (k-1) Cu* adatoms clustered together and f ($f-1$) CO* adsorbates. This definition presumes that a Cu* adatom next to the step edge is always covered by CO*; this is a reasonable assumption from a physical standpoint owing to the high reactivity of Cu* adatoms next to step edges (see Section 6 in Supplementary Material). Similar to eq. (1), $\Delta E^{CO}_{cluster,f} > 0$ indicates a thermodynamic preference for the ejected adatom to remain near the step edge, while $\Delta E^{CO}_{cluster,f} < 0$ indicates a thermodynamic preference for the ejected adatom to aggregate with a pre–existing cluster of k-1 atoms on the Cu(111) terrace. More details are provided in Section 6 of Supplementary Material.

Kinetic Monte Carlo simulation: KMC simulations were performed within the graph–theoretical (GT) framework of Stamatakis and coworkers as implemented in Zacros 2.0 [53–58]. We then provide a brief description of our KMC model. For a more extensive discussion the interested reader is referred to Section 9 of Supplementary Material.

The pristine Cu(111) and the roughened Cu(111) (denoted as R–Cu(111)) surfaces were modeled with a 50 × 50 periodic lattice, which contained two site types, hollow and top (see Figure S14 in Supplementary Material). The number of top sites was 5,000, while the total number of sites was 15,000. The lattice for the Cu(211) surface contained 7,500 sites in total and three site types: (1) top site on the step edge (adsorption site 1 in Figure S3); (2) bridge site on the step edge (adsorption site 2 in Figure S3); (3) and a hollow site between the step edge and the upper terrace (adsorption site 5 in Figure S3).

We modeled CO adsorption/desorption, CO* diffusion, adsorbate–free Cu* and CO*–covered Cu* adatom diffusions that allowed the system to perform a state–to–state random walk (Figure 1 and Table S7). Diffusion events were fast compared to CO* desorption, assuring the fast equilibration of the adsorbate layer. The pre–exponential factors of diffusion events were set two orders of magnitude greater than that for CO* desorption from Cu(111); typical reaction statistics for TPD simulations on R–Cu(111) are presented in Figure S15 and show that diffusion events were indeed significantly faster than CO* desorption throughout simulation. The pre–exponent ratios of diffusion events that involved two different site types were calculated using eq. (S7), thereby assuring the thermodynamic consistency of our calculations (see eq. (S7) and section VI in the Supporting Material of ref. [59]).

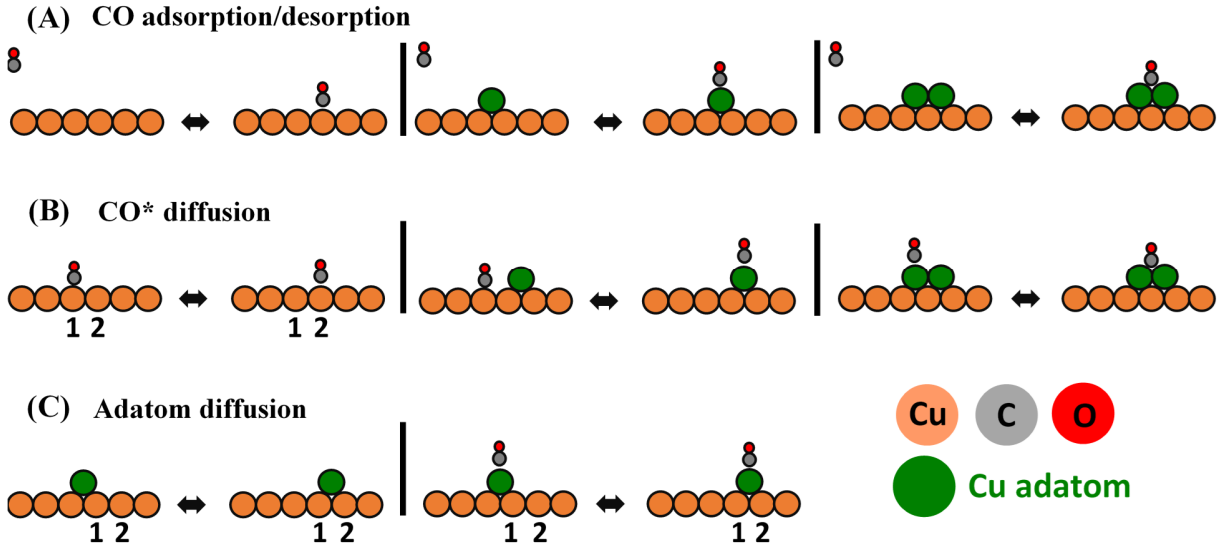

Figure 1. State–to–state events included in the reaction mechanism of the TPD KMC simulations. A full list of events is provided in Table S7. Cu atoms in Cu(111), C, O and Cu* adatoms are shown in orange, grey, red, and green, respectively. Labels '1' and '2' are used to indicate the position of adjacent Cu atoms in Cu(111) in an adspecies diffusion event.

Adsorbate–adsorbate interactions were treated with the cluster expansion (CE) method [60], which was implemented in the GT framework by Stamatakis and coworkers [56]. Surface coverage effects were captured in activation barriers that were computed based on a Brønsted–Evans–Polanyi (BEP) relation [61], similar to previous works [62,63]. Using the CE method, the *Hamiltonian* of any configuration σ ($H(\sigma)$) can be computed based on the energic contribution of certain "figures" (also known as clusters) that are used to compute the lattice energy of σ [59]. To fit the energy of the energetics figures, we performed 134 DFT calculations with nanoclusters of up to seven Cu* adatoms and up to seven CO* adsorbates. Our energetics model contained 23 figures (see Figure S16 and Table S8). The performance of our CE was assessed by means of the leave–one–out cross–validation (CV) score and the root mean square error (RMSE) between DFT and the CE. DFT formation energies were computed according to eq. (S9). There was a good parity between DFT–computed and CE–predicted formation energies (Figure S17). The CV

score and RMSE were 4.0 meV/site and 3.0 meV/site, respectively, suggesting that the predictive power of our CE was adequate.

The R–Cu(111) surface for the KMC TPD was prepared as follows: (1) we sampled a lattice configuration with preexisting Cu* nanoclusters from the stationery region of previous calculations performed at room temperature and 0.30 Torr (0.40 mbar) CO [30]; (2) chemisorbed CO* was completely removed leading to a CO*–free roughened Cu(111) surface; (3) the CO*–free surface from (2) was then exposed to CO gas at T_{ads} = 100 K and P_{CO} =7.50 × 10^{-10} Torr (10^{-9} mbar) up to an exposure slightly more than 1.00 L (L is Langmuir exposure, 1.00 L = 10^{-6} Torr · s); (4) the CO* and Cu* adsorbate layer at 1.00 L was used as the initial input for the TPD simulations (Figure S19). A similar procedure was followed for pristine Cu(111) and Cu(211), with the difference that steps (1) and (2) were omitted as they were not applicable. Similar to R–Cu(111), Cu(211) was exposed to 1.00 L of CO, while Cu(111) was exposed to 0.40 L at 100 K and P_{CO} =7.50 × 10^{-10} Torr (10^{--9} mbar). The smaller exposure for Cu(111) assured the absence of regions of high local CO* coverage. Such regions lead to loosely bound CO* in numerous 1st nearest neighbor patterns. CO* tends to desorb easily from these configurations owing to CO*–CO* repulsive interactions, thereby giving rise to an additional low temperature TPD peak at 119 K (see Figure S21). The temperature was always ramped linearly at 3 K/s between 100 K and 300 K. During TPD simulations, the partial pressure of CO gas was negligibly small (7.5 × 10^{-22} Torr or 10^{-10} mbar). The R–Cu(111) surface contained a fixed number of 850 Cu* adatoms, which corresponds to 0.17 of a monolayer (ML) coverage of Cu(111). We assumed a fixed number of pre–existing adatoms on Cu(111) because the goals of this work were:(1) to showcase how surface restructuring and surface–adsorbate bond breaking can be coupled in KMC simulations; (2) to provide an initial assessment of TPD as a method for the detection of metal

nanoclusters. The ejection of Cu atoms from step edges was not included in the reaction mechanism of the present KMC simulations, but it was considered in a recent study [30]. TPD spectra presented in section 3.3 were obtained by averaging the results of ten KMC simulations at identical conditions.

3. Results and discussion

3.1. The reactivity of small nanoclusters over Cu(111)

The adsorption of CO and other adsorbates on pristine Cu(111) has been extensively studied in a previous DFT work [64]. Here, we elucidate the reactivity of small nanoclusters on Cu(111) by studying the adsorption of CO thereon. We denote nanoclusters as Cu_x/Cu(111), where x is the number of Cu* adatoms in the nanocluster and assumes values between one and seven ($1 \leq x \leq 7$). Figure 2 (A) shows the most stable CO* adsorption geometries on Cu_x/Cu(111) clusters. CO* adopts a C–down perpendicular adsorption structure on Cu_1/Cu(111). This geometry maximizes the overlap between the 5σ and 2π* CO* orbitals and the metal states [65]. On $Cu_{2\leq x\leq 7}$/Cu(111), CO* is tilted due to its interaction with copper atoms both in the cluster and in the Cu(111) surface [19,66].

According to our data, for all x studied, there is a strong CO*–Cu_x/Cu(111) interaction that is at least 0.25 eV stronger than the CO*–Cu(111) interaction ($\Delta E_{ads}(CO*) = -0.50$ eV) (Figure 2 (B)). Our predicted CO* adsorption geometries and adsorption energies are in good agreement with previous DFT studies [66], and the difference in the CO* binding strength between Cu(111) and nanoclusters underscores the high reactivity of the latter (Figure 2 (B)).

To clarify whether the enhanced adsorbate–nanocluster interaction is specific to CO*, we studied the adsorption of other species on Cu_x/Cu(111). We computed the adsorption energies of

N*, O*, H*, NO*, N_2* and N_2O* on $Cu_{1\leq x\leq 7}$/Cu(111) and compared them with the corresponding values for pristine Cu(111) and Cu(211) (Figure 2 (C) and (D)). Given that the PBE+U approach is tailored to the chemisorption of CO* on Cu(111) [19], the adsorption energies of N*, O*, H*, NO*, N_2* and N_2O* were computed using the PBE exchange and correlation functional. Despite the possible error with PBE in predicting the adsorbate–metal interactions, the aim of these calculations is not to reproduce experimentally obtained adsorption energies, but rather to highlight differences in the reactive nature of Cu_x/Cu(111) compared to pristine Cu(111) and Cu(211).

Regarding the most stable adsorption sites, N*, O*, H*, and NO* prefer to adsorb on hollow fcc or hcp sites on both Cu(111) and Cu_x/Cu(111) (Figure S9 and Figure S10), while N_2* always prefers perpendicular atop adsorption (Figure S10). For N_2O* we consider two different adsorption structures: (i) an adsorption mode with N_2O* interacting with a Cu atom through its terminal nitrogen (N_t) and (ii) an adsorption mode where both N_t and the O atom interact with Cu (Figure S8). These adsorption geometries are denoted as $\eta_1\{N_t\}$ and $\eta_2\{N_t,O\}$ respectively, and are important because $\eta_1\{N_t\}$ is usually the first adsorption geometry adopted upon N_2O–metal interaction [67], while $\eta_2\{N_t,O\}$ is the precursor geometry for the dissociation of N_2O* to N_2* and O* [68].

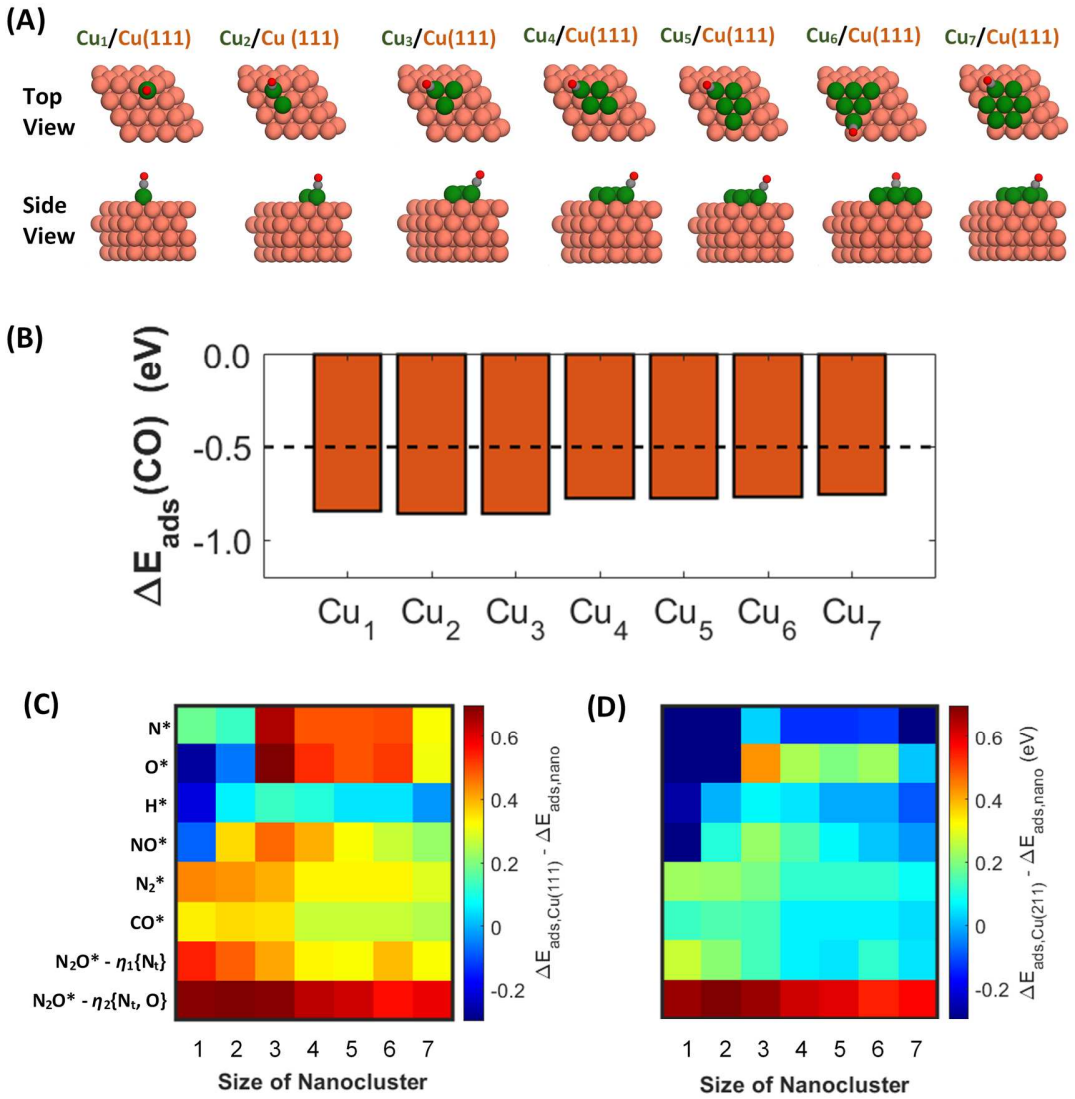

Figure 2. (A) Top and side views of optimized CO* adsorption geometries on Cu* nanoclusters. C, O, and Cu atoms are shown in grey, red and orange, respectively. Cu adatoms are shown in green. (B) PBE+U computed CO* adsorption energies ($\Delta E_{ads}(CO*)$) on Cu* nanoclusters. The horizontal black dashed line denotes the adsorption energy of CO* on Cu(111) computed with the PBE+U method. (C) Adsorption energy differences between adsorption on Cu(111) and Cu_x/Cu(111) ($\Delta E_{nano,ads}$). (D) Adsorption energy differences between adsorption on Cu(211) and Cu_x/Cu(111) ($\Delta E_{ads,nano}$). For panels D and E, red color indicates stronger binding of the adsorbate on the nanocluster compared to the Cu(111) and the Cu(211) surfaces, respectively.

Figure 2 (C) and (D) show $\Delta E_{ads,Cu(111)} - \Delta E_{ads,nano}$ and $\Delta E_{ads,Cu(211)} - \Delta E_{ads,nano}$ ($\Delta E_{ads,nano}$ denotes the adsorption energy on nanoclusters) values for the adsorbate species considered in this study. These values indicate whether adsorbate binding is stronger on the

pristine Cu(111) and Cu(211) surface or on Cu* nanoclusters: negative values imply stronger binding on Cu(111) or Cu(211), whilst positive values imply stronger binding on Cu* nanoclusters. The adsorption energies of adspecies on Cu(211), Cu(111) and Cu_x/Cu(111) are summarized in Table S3, Table S4, and Table S5, respectively.

The binding of the species studied on Cu_x/Cu(111) is, on average, stronger than that on Cu(111) and Cu(211) by ca. 0.34 eV and 0.10 eV, respectively (Figure 2 (C) and (D)). We note that atomic species interact more weakly with Cu_1/Cu(111) and Cu_2/Cu(111) than with Cu(111) and Cu(211). This might be explained by the preference of N*, O*, and H* for high symmetry hollow sites that are not found in clusters with less than 3 Cu atoms. In particular, N* interacts more strongly with Cu(211) than with Cu_x/Cu(111) irrespective of the nanocluster size ($\Delta E_{ads,Cu(211)} - \Delta E_{ads,nano} < 0.0\ eV$ – Figure 2 (D)). This is because N* adsorbs and interacts strongly with a high symmetry fourfold hollow site between the step edge and the lower terrace on Cu(211) (Figure S13). A similar behavior is observed for NO*, but clearly not for N_2* which binds always stronger on top sites (Figure 2 (D) and Figure S10 (A)). Yet, $\Delta E_{ads,Cu(111)} - \Delta E_{ads,nano}$ values for atomic species and NO* become positive on Cu_x/Cu(111) with x > 2. The most positive values are generally observed for x = 3 (Figure 2 (C) and (D)) underscoring the remarkable reactivity of Cu_3/Cu(111) trimer clusters. Cu_3/Cu(111) clusters have shown optimal activity toward the catalytic oxidation of CO [30].

Finally, N_2O*, in both $\eta_1\{N_t\}$ and $\eta_2\{N_t,O\}$ adsorption geometries, interacts considerably more strongly with Cu_x/Cu(111) than with Cu(111). $\Delta E_{ads,Cu(111)} - \Delta E_{ads,nano}$ is always greater than 0.31 eV (Figure 2 (C)). A similar trend is observed for Cu(211), where in most cases $\Delta E_{ads,Cu(211)} - \Delta E_{ads,nano}$ > 0.10 eV (Figure 2 (D)). The enhanced N_2O*–Cu_x/Cu(111) interaction is practically important as N_2O* dissociation to N_2* competes with N_2O* desorption

on metal surfaces [68,69]. Because of this enhanced interaction, roughened Cu surfaces could be much more efficient in decomposing N_2O* to N_2 than pristine surfaces.

3.2. Cu atom ejection from Cu(211)

3.2.1. Vacuum and near vacuum conditions

Having assessed the reactivity of small Cu* nanoclusters on Cu(111), we proceed by investigating the ejection of Cu atoms from Cu(211) step edges that may subsequently aggregate over Cu(111) terraces to form clusters. The ejection events occur in step edge sites of Cu(111) single crystals and result in an initial roughening of the step edge vicinity before nanocluster formation on adjacent Cu(111) terraces [18,19]. To model such sites, we use the Cu(211) surface that contains a step edge connected with a lower and an upper terrace (Figure S1).

We first study the thermodynamics and kinetics of Cu step edge atom ejection in vacuum (i.e., in the absence of any adsorbates). Under these conditions, we identify three ejection pathways, with one of them being concerted (Figure S2). Figure 3 (A) shows the most thermodynamically and kinetically favorable pathway, where a Cu atom is ejected from the step edge to the lower Cu(211) terrace. The activation energy for this ejection pathway is 0.92 eV, which assuming a prefactor of 10^{13} s^{-1}, yields a rate of 2.76×10^{-3} s^{-1} at room temperature. Additionally, the ejection event is endothermic (ΔE_{rxn} = +0.85 eV), and therefore we predict that Cu(111) roughening will be limited in vacuum.

Next, we perform the same calculations in the presence of a single CO* adsorbate that corresponds to a coverage of ca. 0.08 ML (Figure 3 (B)). These conditions correspond to ultra–low CO pressures where small CO* coverages are observed. While CO* may adsorb on different sites on the Cu(211) surface (Figure S3 and Table S1), the PBE+U approach indicates that the

most stable adsorption structure involves CO* perpendicularly adsorbed on a top site of the step edge (Figure S3). The calculated adsorption energy for atop adsorption on the step edge is –0.71 eV in excellent agreement with prior DFT calculations of Gajdoš *et al.* [70] ($\Delta E_{ads}(CO*)$ = –0.72 eV) and in reasonable agreement with the low–coverage temperature desorption experiments of Vollmer *et al.* ($\Delta E_{ads}(CO*)$ = –0.61 ± 0.014 eV) [47].

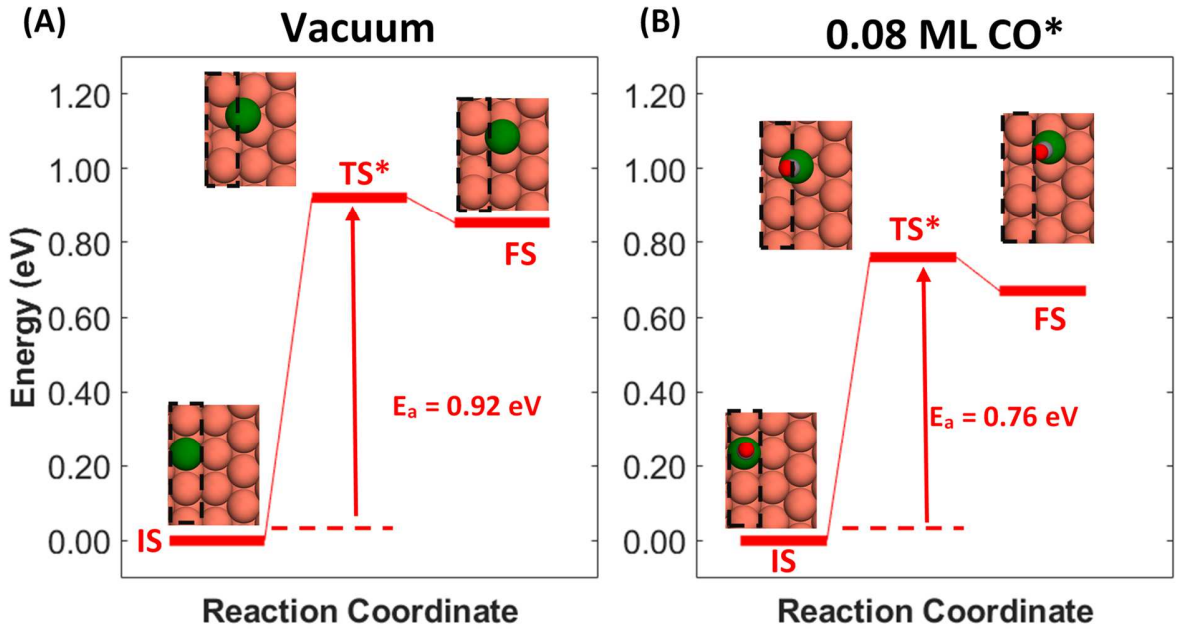

Figure 3. Calculated potential energy diagrams for Cu atom ejection (A) in vacuum and (B) at a low CO* coverage of 0.08 ML. Cu atoms involved in the ejection event are shown in green. Other Cu atoms are shown in orange. C and O are shown in grey and red, respectively. Inset values are the calculated activation energies (E_a); all energies are referenced to the energy of the initial state (IS). TS and FS stand for transition state and final state, respectively. Dashed black rectangles show the position of the step edge in Cu(211).

The presence of 0.08 ML CO* facilitates Cu ejection from the step by reducing the ejection barrier from 0.92 eV to 0.76 eV (Figure 3 (B)), thus increasing the reaction rate by approximately three orders of magnitude at room temperature (from 2.76×10^{-3} s^{-1} to 1.40 s^{-1}). However, the Cu atom ejection step remains significantly endothermic (ΔE_{rxn} = +0.68 eV) and therefore "effective" ejections of Cu atoms will be rare at room temperature and low CO*

coverages. Consequently, ejected Cu atoms will tend to recover their initial positions in the step edge. This conclusion is congruent with the experimental work of Baran *et al.* where at CO pressures less than 0.10 Torr ($\leq$ 0.06 ML) the terraces of Cu(111) were reported atomically flat without the presence of Cu* nanoclusters [19].

3.2.2. CO* coverage effects

Given that ejection events will be rare under conditions near ultra–high vacuum (UHV), we next examine the effect of higher CO* coverages on the kinetics and thermodynamics of Cu atom ejection from step edges. To define a realistic CO* coverage range for our study, we compute CO* differential adsorption energies ($\Delta E_{diff}(CO*)$) at different surface coverages (Figure 4 (A)). These calculations provide an approximate guess for the CO* saturation coverage beyond which the adsorption of CO species on Cu(211) becomes thermodynamically unfavorable.

We first calculate $\Delta E_{diff}(CO*)$ on Cu(111) because the CO/Cu(111) system has been the subject of numerous studies [43, 69–71], and is appropriate for benchmarking our calculations. We report $\Delta E_{diff}(CO*)$ for the most stable CO* adlayers at different coverages (see Figure S4 and Figure S5). At 0 K, $\Delta E_{diff}(CO*)$ remains negative up to a CO* coverage of 0.56 ML but assumes significantly positive values (> 0.70 eV) for higher CO* coverages (Figure 4 (A)). Our estimated saturation coverage of 0.56 ML agrees well with earlier DFT calculations (0.55 ML in a $p(3 \times 3)$ slab) [74] and surface science experiments on Cu(111) (0.52 ML) [48].

The same type of calculations was then repeated for Cu(211) and the obtained estimate for the CO* saturation coverage is 0.50 ML (Figure 4 (A)). Yet, we note that at 0.58 ML, $\Delta E_{diff}(CO*)$ is not excessively positive ($\approx$ 0.20 eV), thereby indicating that coverages close to

0.58 ML might be possible at high chemical potentials of CO gas. Accordingly, in the following text we explore CO* coverages that range between 0.08 ML and 0.58 ML on Cu(211).

To evaluate the importance of CO* coverage effects, we consider two restructuring events. The first is the ejection of a Cu atom from the step edge of Cu(211) (Figure 4 (C) – **IS** → **FS$_1$**), and the second is a hopping diffusion of an adjacent Cu atom in the step edge moving along the step edge to heal the vacancy generated by the ejection step (Figure 4 (C) – **FS$_1$** → **FS$_2$**). The kinetics of the latter step provide an indication of how fast step edges restructure under reactive environments and how fast generated vacancies might be annihilated by neighboring step edge Cu atoms.

We present potential energy diagrams for three different CO* coverages on Cu(211) that are representative of low, intermediate, and high CO* coverages: 0.08 ML, 0.33 ML and 0.58 ML, respectively (Figure 4 (D)). A key observation is that CO* coverage effects have an important effect on the thermodynamics and the kinetics of both restructuring events (Figure 4 (D)). First, the reaction energy of Cu atom ejection is +0.68 eV, +0.40 eV and +0.32 eV for 0.08 ML, 0.33 ML and 0.58 ML CO* coverages, respectively, suggesting that large CO* coverages facilitate the thermodynamics of Cu atoms ejection. Second, the barrier for Cu atom ejection (**IS** → **FS$_1$**) is decreased by 0.37 eV when the CO* coverage increases from 0.08 ML to 0.58 ML (Figure 4 (D)). Such barrier reduction corresponds to approximately a six orders of magnitude increase in the ejection rate at room temperature (rates of 1.04 s^{-1} and 1.76 × 10^6 s^{-1} for 0.08 ML and 0.58 ML, respectively), thereby rationalizing why Cu(111) roughens only in the presence of CO and not under vacuum conditions [19].

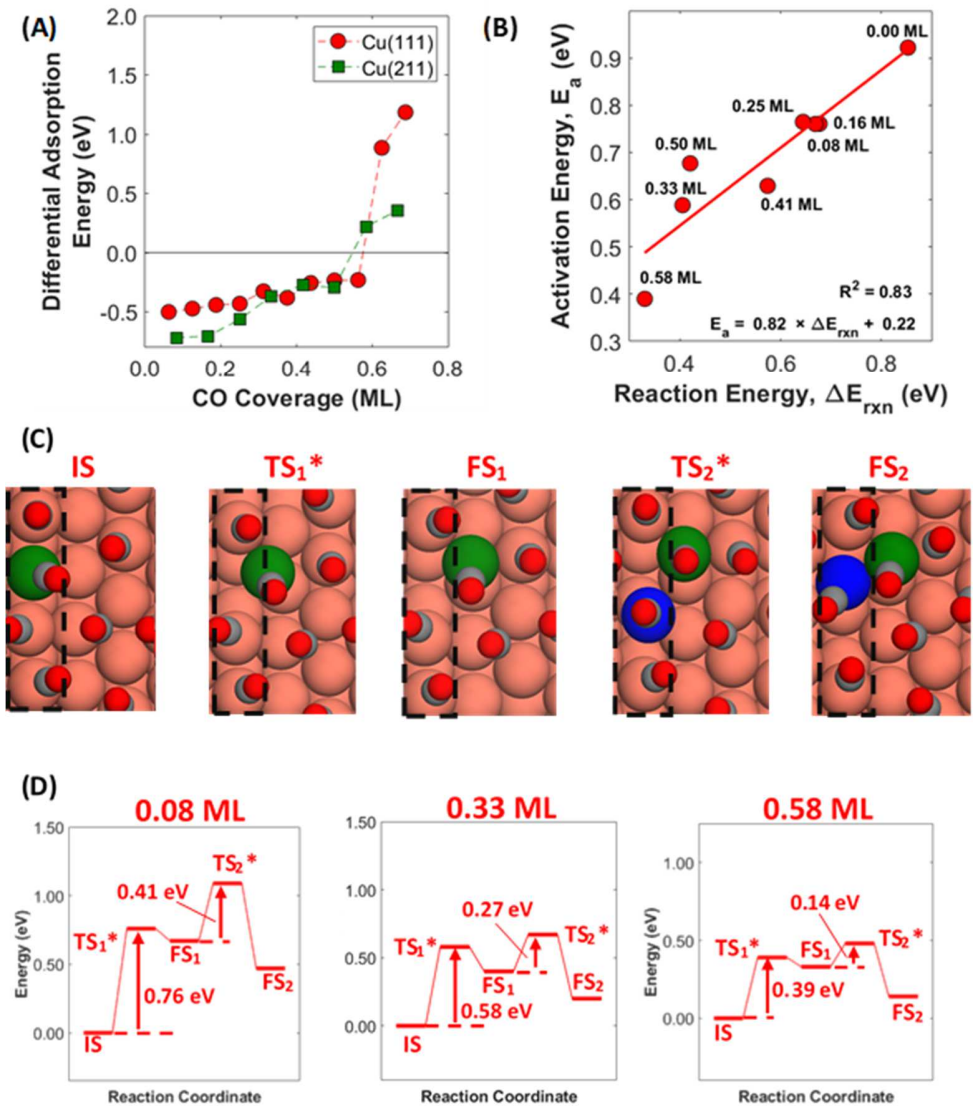

Figure 4. (A) CO* differential adsorption energies for different CO* surface coverages on Cu(111) and Cu(211). (B) Brønsted–Evans–Polanyi relation for the ejection of a Cu atom from the step edge of Cu(211). The activation energy, E_a, is defined as the difference in energy between the TS and IS energies (TS_1* and IS in panel (D)) of the ejection event. The reaction energy, $\Delta E_{rxn,}$ is defined as the difference between the FS and IS energies of the ejection event (FS_1 and IS in panel (D)). The red line is the linear regression line. The slope, intercept, and determination coefficient (R^2) are shown in the bottom of the plot. (C) Top view of states involved in the computed potential energy diagrams that include ejection and diffusion of a Cu atom in the step edge for a CO* coverage of 0.58 ML. Cu, O, and C atoms are shown in orange, red, and grey, respectively. Cu atoms involved in the ejection and diffusion events are shown in green and blue, respectively. Step edges of Cu(211) are indicated by dashed rectangles. (D) Potential energy diagrams for CO* coverages of 0.08 ML, 0.33 ML, and 0.58 ML. Numbers represent activation energies in units of eV, with the energies of all states referenced to the energy of the initial state.

Similar to the Cu atom ejection kinetics, the hopping diffusion of Cu atoms in the step edge (**FS_1 → FS_2** in Figure 4 (C)) becomes faster at increasing CO* coverages. The computed

barriers for this event are 0.41 eV, 0.27 eV and 0.14 eV for 0.08 ML, 0.33 ML and 0.58 ML (Figure 4 (D)), respectively. These low barriers lead to high diffusion rates at room temperature ($> 10^5$ s^{-1} even for a barrier of 0.41 eV) and reveal the dynamic nature of step edges during catalysis. At intermediate CO* coverages (0.33 ML), where Cu atom ejection is kinetically facile (barrier 0.58 eV) but remains endothermic (+0.40 eV), one should expect the formation of a number of adatoms in the vicinity of the step edge. These adatoms are ejected and, possibly, it becomes increasingly difficult for them to reassume their initial positions in the step edge owing to the fast annihilation of vacancies by diffusing atoms across the step edge. Note that at 0.08 ML, the kinetic barrier for the reverse event to Cu ejection is just 0.10 eV, which is significantly smaller to the vacancy annihilation (via step atom diffusion) barrier, 0.41 eV (Figure 4 (D)). By contrast, at 0.33 ML the difference between the former and the latter barriers is less than 0.10 eV different, 0.18 eV and 0.27 eV, respectively (Figure 4 (D)). Roughening of step edges has been experimentally observed at 0.10 Torr, namely a slightly lower pressure than the onset pressure for the formation of nanoclusters [19].

Besides the three CO* coverages shown in Figure 4 (D), we study the thermodynamics and kinetics of Cu atom ejection for other possible coverages in the range of 0.00 ML – 0.58 ML (Figure 4 (B)). Based on these data, we determine that there exists a Brønsted–Evans–Polanyi (BEP) relation (Figure 4 (B)) [75–77], whereby the ejection activation barrier scales linearly with the reaction energy for the ejection step. The computed slope is close to unity (slope = 0.82), and therefore is indicative of a late transition state. This is in line with geometries displayed in Figure 4 (C) and Figure S6, where the TS structures (TS1*) resemble the respective FS structures (FS1*). Importantly, the obtained BEP relation corroborates that increasing CO* coverages

facilitate, thermodynamically and kinetically, the ejection of Cu atoms from step edges, a result in excellent qualitative agreement with experiment [19].

3.2.3. Thermodynamic stability of ejected Cu atoms

Next, we examine the tendency of Cu* adatoms to remain in the vicinity of the step edge after ejection as opposed to migrating to the Cu(111) terrace and subsequently aggregate with preexisting clusters/adatoms. We adopt a thermodynamic approach that should be adequately accurate thanks to the fast kinetics of Cu* adatom diffusion *via* hopping on Cu(111), characterized by a barrier $E_a < 0.15$ eV [78,79].

We calculate cluster formation energies at three conditions (see Section 2 in main text and Section 6 in Supplementary Material): (a) vacuum; (b) intermediate CO* coverages; and (c) high CO* coverages. Under vacuum, the DFT slabs are clean of adsorbates and eq. (1) is used to compute cluster formation energies. High coverages simulate high CO chemical potentials, and the CO* coverage on Cu(211) in the initial state is set to 0.50 ML, which is the highest coverage for which $\Delta E_{diff}(CO*) < 0$ (Figure 4 (A)). In this case, the cluster formation energy is computed using eq. (2) by setting f = k that corresponds to nanoclusters fully covered by CO* (one CO* per Cu* adatom on Cu(111)). This assumption is realistic and thermodynamically consistent given the high reactivity of small clusters (Figure 2 (A)), and that, $\Delta E_{diff}(CO*)$ remains negative even for CO* fractional coverages equal to one (see Table S6). At intermediate coverages, nanoclusters on Cu(111) are partially covered by CO* and the initial coverage of Cu(211) is set at 0.33 ML (see Section 6 in the Supplementary Material for more information).

Figure 5 shows $\Delta E^{Vac}_{cluster,f}$ for small clusters of different sizes. $\Delta E^{Vac}_{cluster,f}$ is positive for Cu clusters with four atoms or less, while it becomes negative for clusters with five atoms or more. In the absence of CO* the ejection of Cu atoms is highly endothermic and slow, and thus can be

expected to be rare at room temperature (Figure 3 (A)). Accordingly, the formation of clusters with more than four atoms that can stabilize newcomer adatoms will be unlikely in vacuum (Figure 5).

At intermediate and high CO* coverages, $\Delta E^{CO*}_{cluster,f}$ is negative for clusters with three atoms or more on Cu(111) ($\Delta E^{CO*}_{cluster,f}$ = –0.06 eV and –0.02 eV for high and intermediate CO* coverages, respectively). Under these circumstances, there is a thermodynamic driving force for isolated adatoms in the step edge to migrate to Cu(111) and aggregate with preexisting dimers to form trimers. The latter are the smallest clusters to exhibit negative $\Delta E^{CO*}_{cluster,f}$ for intermediate CO* coverage (at high coverages even dimers exhibit a small negative $\Delta E^{CO*}_{cluster,f}$ of –0.005 eV). This observation is congruent with HP–STM that has confirmed the temporary stability of trimers on terraces of Cu(111) under CO atmospheres [19], but not the stability of isolated adatoms and dimers, which according to our analysis appear as metastable clusters with short lifetimes.

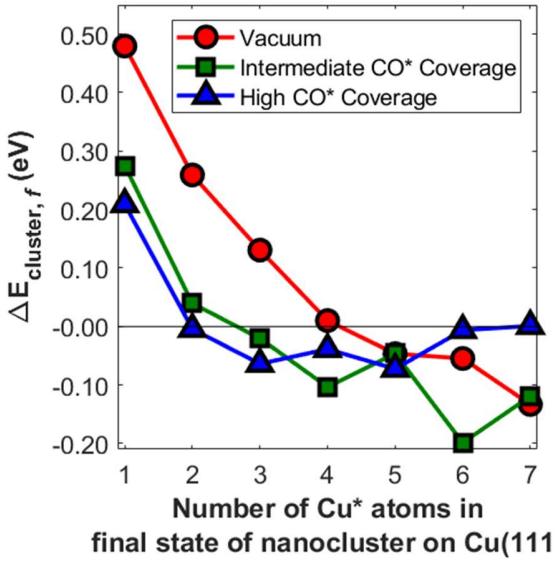

Figure 5. Computed cluster formation energies ($\Delta E_{\mathrm{cluster},f}$) in vacuum, intermediate and high CO* coverage. The x–axis shows the final nanocluster size on Cu(111) after migration of an ejected Cu atom

from the step edge of Cu(211) (for definitions see eq. (1), eq. (2) in main text and Section 6 in the Supplementary Material).

Therefore, our results thus far reveal that CO* coverage effects not only provide a driving force for the ejection of Cu atoms from the step edges, but also for the migration of adatoms from the Cu step edge to Cu(111) terraces for the formation of Cu clusters thereon. These effects are important and should be taken into account for modeling surface reactions [80,81], and for determining the structure of metal surfaces in the presence of reactive environments [30].

3.3. CO* desorption from roughened Cu surfaces: KMC simulations of TPD

To further interrogate the reactivity of Cu* nanoclusters on Cu(111), we model and analyze CO* desorption from roughened Cu(111) (R–Cu(111)) by means of TPD KMC simulations. The same desorption process is modeled on Cu(111) and Cu(211), which serve as a comparison to desorption from R–Cu(111) and assist with the validation of our data. KMC simulation of TPD is valuable for rationalizing data derived from experiments. This method can largely deal with the complexity of real surfaces by allowing the explicit treatment of adsorbate–adsorbate interactions and of surface heterogeneity. In the context of this work, these simulations also provide an initial evaluation of TPD as a method for the detection of nanoclusters on metal surfaces.

Figure 6 (A) and (B) show simulated TPD spectra for CO* desorption from Cu(111) and Cu(211). The reaction mechanism for the pristine surfaces involves CO* diffusion and CO* desorption events, while CO* adsorption was prevented by assigning gas phase CO with a negligible partial pressure of (see Section 2 and Figure 1). CO*–CO* interactions of up to third and second nearest neighbor were included in the energetics model of Cu(111) and Cu(211) (Figure S16 and Figure S18).

The TPD spectrum for the pristine Cu(111) surface shows a broad peak, spanning from 127 K to 184 K, where two maxima occur at T_p = 152 K and T_p = 166 K (Figure 6 (A)). The shape of the peak can be rationalized by the effect of CO*–CO* interactions that cause the transition of the CO* adlayer from an ordered structure at "high" CO* coverage (θ_{CO*} > 0.12 ML) to an increasingly disordered structure at surface temperatures greater than 155 K or θ_{CO*} < 0.09 ML (Figure S20). In our CO* TPD simulations, coverage–dependent activation energies for CO* desorption from a lattice configuration of neighboring adsorbates σ, are computed based on a BEP relation assuming a proximity factor equal to zero [56]: $\mathrm{E}_{des,CO*}(\sigma) = max\left\{-\Delta \mathrm{E}_{rxn}(\sigma), 0, \mathrm{E}_{des,0} - (\Delta \mathrm{E}_{rxn}(\sigma) - \Delta \mathrm{E}_{rxn,0})\right\}$, where $\mathrm{E}_{des,0}$ is the CO* desorption energy and $\Delta \mathrm{E}_{rxn,0}$ is the reaction energy for the *adsorption of CO* from the gas phase to the surface at the zero coverage limit; $\mathrm{E}_{des,CO*}(\sigma)$ and $\Delta \mathrm{E}_{rxn}(\sigma)$ are the same parameters but in their coverage–cognizant form, whereby the energetic effect of the local adlayer structure from where the CO* desorption occurs is taken into account; the proximity factor is a parameter that assumes values between 1.0 for product–like transition states and zero for reactant–like transition states [82]. CO*–CO* adsorbate interactions result in less negative $\Delta \mathrm{E}_{rxn}(\sigma)$ values. Accordingly, low CO* coverages result in larger $\mathrm{E}_{des,CO*}(\sigma)$ compared to high CO* coverages and therefore to desorption peaks appearing at higher temperature because of less extensive CO*–CO* repulsions. The second desorption peak, at 166 K, corresponds to CO* desorption from a low surface coverage regime (θ_{CO*} < 0.09 ML – Figure 6 (A)). This peak desorption temperature is in good agreement with the experiments of Kirstein et al. where the main desorption peak was observed at 173 K when Cu(111) was exposed to 0.3 L of CO at 105 K and the temperature was ramped at 0.7 K/s [71].

Regarding Cu(211), our data show a single and well–defined desorption peak with a maximum at 219 K (Figure 6 (B)). The initial CO* surface coverage is 0.34 ML, while the surface coverage at which the peak occurs is 0.14 ML. Under the conditions of our simulations, the dominant adsorption site is the top site in the step edge, while CO* adsorbed on the step edge bridge and the hollow site between step edge and its adjacent upper terrace are negligible. Vollmer et al. performed CO* thermal desorption spectroscopy on dilute CO* adlayers on Cu(211) with a temperature ramp rate of 5 K/s [47]. The main desorption peak appeared at approximately 240 K, which is shifted to higher temperature by 21 K compared to our prediction (Figure 6 (B)) [47]. In the same study, the main Cu(111) CO* desorption peak was reported at 189 K being shifted by a similar amount (23 K) as for Cu(211) compared to the low CO* coverage peak in our data (Figure 6 (A)) [47]. Therefore, our DFT–based KMC results seem to capture correctly the stronger interaction of CO* with the step edges of Cu(211) compared to pristine Cu(111) (Figure 6 (A) and (B)) and provide consistent results on a qualitative basis.

Next we perform CO* TPD simulations on the roughened Cu(111) (R–Cu(111)), which includes clusters of Cu atoms generated by the ejection of Cu atoms from undercoordinated step edges followed by Cu* adatom aggregation on Cu(111). It should be noted these simulations account for CO*–CO* interactions, and combine surface restructuring (i.e., Cu* adatom diffusion) with surface–adsorbate reactions that involve bond breaking (i.e., CO* desorption). Namely, they account for effects that contribute to the high complexity of surface reactions an are occasionally fundamental for the development of accurate computational models. Cu* adatom diffusion allows nanoclusters with a specific number of adatoms to assume numerous geometries during simulation before evolving into larger nanoclusters. Such isomeric structures

might exhibit disparate catalytic behavior, which can be investigated using our *ab initio* KMC approach.

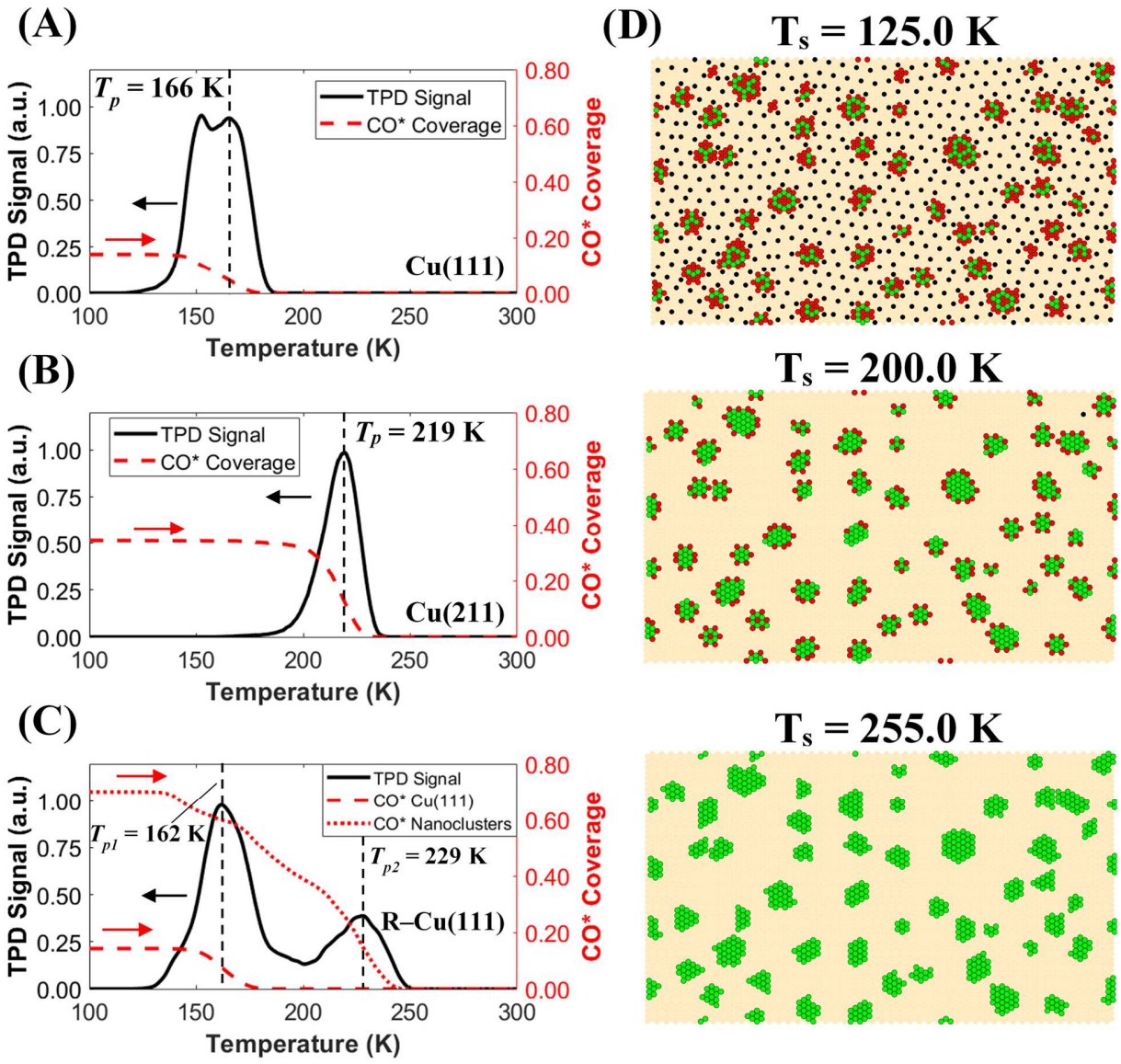

Figure 6. KMC CO* TPD spectra for: (A) pristine Cu(111) – 0.40 L CO exposure; (B) pristine Cu(211) – 1.00 L CO exposure; and (C) a roughened C0u(111) (R–Cu(111)) by Cu* nanoclusters – 1.00 L CO exposure. The Cu(211) surface contained 7,500 sites in total with 2,500 top sites, 2,500 bridge sites and 2,500 hollow sites formed between the upper terrace and the step edge. The CO* coverage of the pristine surfaces is defined simply as the total number of surface atoms covered by CO* divided by the total number of surface atoms, while for R–Cu(111) we plot the total CO* coverage on Cu* nanoclusters (eq. (S10) – CO* Cov. CuAd*) and on Cu(111) domains separately (eq. (S11) – CO* Cov. Cu). (D) KMC snapshots at different stages of the CO* TPD simulation for R–Cu(111). The snapshot at 125 K resembles to the adlayer obtained after exposure to CO at 100 K and corresponds to the adlayer structure right before CO* desorption begins from the roughened surface. Cu* adatoms, Cu atoms in Cu(111) are shown

as light green and light orange circles, respectively. Cu* adatoms and Cu atoms in Cu(111) *covered by* CO* are shown as red and black circles.

The simulated TPD spectrum for CO* desorption from the R–Cu(111) model surface exhibits two distinct peaks with maxima at T_{p1} = 162 K and T_{p2} = 229 K (Figure 6 (C)). Figure 6 (D) shows KMC snapshots at three different temperatures verifying that the lower temperature peak (T_{p2} = 162 K) is associated with CO* desorption from Cu(111) domains not covered by Cu* nanoclusters on R–Cu(111), while the higher temperature peak (T_{p2} = 229 K) is associated with CO* desorption from Cu* edge atoms in nanoclusters. In addition, CO* adsorbed on center Cu* nanocluster atoms are desorbed below 200 K, along with CO* desorbing from Cu(111) domains of the R–Cu(111) surface (Figure 6 (C))

Using HP–STM at 0.20 Torr CO pressure and room temperature, Salmeron and coworkers observed hexagonal shaped Cu* clusters with CO* molecules adsorbed on their periphery [19]. This observation agrees well with our simulation results that demonstrate the reactivity of Cu* edge sites in nanoclusters and sample geometrically similar configurations to HP–STM (Figure 6 (C) and (D)). These strongly bound CO* adsorbed on the periphery undercoordinated sites of nanoclusters give rise to the second desorption peak (T_{p1} = 229 K), which is shifted by 10 K to higher temperature than the Cu(211) peak (T_p = 219 K – Figure 6 (B) and (C)). Accordingly, R–Cu(111) appears to exhibit dramatically higher adsorption affinity for CO* compared to Cu(111), but also higher adsorption affinity for CO* than Cu(211). It is noteworthy that the step edge sites of Cu(211) bind CO* more strongly than other single crystals with step edges and kinks (Cu(221) and Cu(532)), and also stronger compared to polycrystalline surfaces that serve as a model for industrial Cu catalysts [47]. Therefore, our work suggests that TPD can be a promising method for the detection of metal nanoclusters over metal surfaces.

We close this section by discussing the importance of adsorbate–adsorbate interactions. As noted earlier in this section, activation energies in our simulations are coverage–dependent and coverage effects are accounted for by BEP relations. The inverse Wigner–Polanyi equation (eq. (3)) is commonly used in experimental surface science and provides mean–field coverage–dependent desorption energies [83]:

$$\mathrm{E}_{des,CO*}(\theta) = -R\,T\,\ln\left(-\frac{\left\{{}^{d\theta_{CO*,clusters}}/_{dt}\right\}_{KMC}}{A(T)\,\theta^{n}}\right), \qquad (3)$$

where $A(T)$ is the pre-exponential coefficient and can be calculated from first–principles (eq. (S4) in Section 9 of the Supplementary Material); n is the desorption order. Assuming a first order desorption and using eq. (3), we calculate $\mathrm{E}_{des,CO*}(\theta)$ for R–Cu(111) at temperatures higher than 200 K where CO* desorption from the nanocluster periphery sites begins to happen (Figure 7 (A)). We find that $\mathrm{E}_{des,CO*}(\theta)$ increases monotonically from ca. 67.0 kJ/mol to ca. 72.0 kJ/mol as the *nanocluster CO* coverage* decreases from 0.38 ML to almost zero. At 0.38 ML nanocluster coverage, there is no CO* on the Cu(111) domains of R–Cu(111), yet there is significant amount of chemisorbed CO* on undercoordinated sites of the periphery of nanoclusters (see Figure 6 (C) and middle snapshot of panel (D) in same figure). Interestingly, the highest $\mathrm{E}_{des,CO*}(\theta)$ close to the zero coverage limit closely matches $\Delta\mathrm{E}_{\mathrm{ads}}(\mathrm{CO}*)$ on the edge site of Cu* heptamer clusters (–0.75 eV or –72.4 kJ/mol – Figure 2 (B)).

Moreover, we record $\mathrm{E}_{des,CO*}(\theta)$ values for desorption events, which occurred beyond 200 K. The corresponding distribution is shown in Figure 7 (B). These desorption activation energies are representative of CO* desorption events occurring from undercoordinated edge sites of Cu* nanoclusters like these shown in the middle KMC snapshot of Figure 6 (D). As observed, the largest fraction (slightly more than ¼) of CO* desorption events occur with $\mathrm{E}_{des,CO*}(\theta)$ of

approximately 72.0 kJ/mol, while values lower and higher than that are also recorded. The wide range of $E_{des,CO*}(\theta)$ is attributed to the surface heterogeneity caused by nanoclusters of various geometries that undergo dynamic restructuring during simulation, but also to local coverage effects because of CO*–CO* interactions. This result demonstrates the power of the KMC method in modeling reactions over solid surfaces that, in practice, are not static when exposed to strongly bound adsorbates and elevated temperatures.

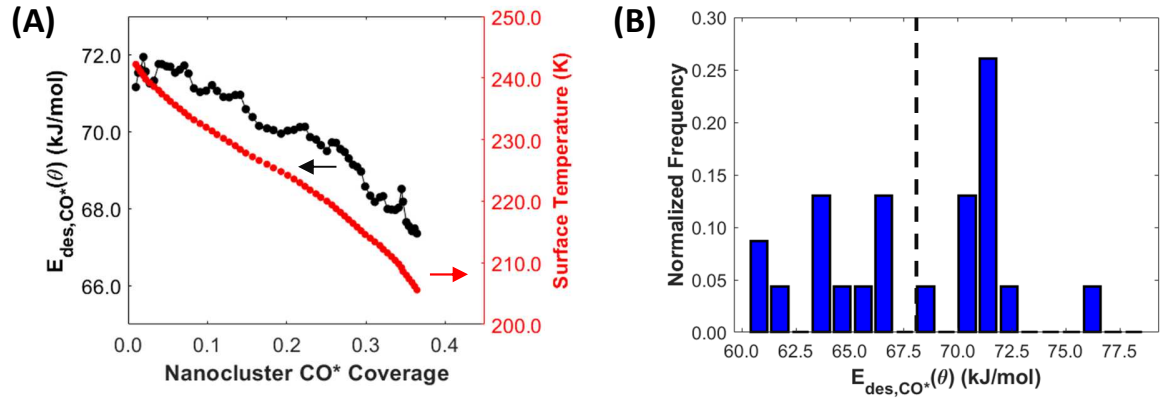

Figure 7. (A) Coverage–dependent activation energies for CO* desorption ($E_{des,CO*}(\theta)$) obtained by the inversed Polanyi–Wigner equation. For the definitions of CO* coverage on R–Cu(111) see Section 9 in the Supplementary Material. (B) Distribution of CO* desorption activation energies ($E_{des,CO*}(\theta)$) obtained from KMC for surface temperature higher than 200 K. A dashed black line indicates the DFT–computed atop CO* adsorption energy on the step edge of Cu(211). The data presented in panel (B) require recording of every single event occurring during simulation and could lead to too big simulation output files. To obtain these data avoiding the generation of too large Zacros output files, an additional KMC simulation was performed where the initial temperature was 150 K and there was no CO* adsorbed on the Cu(111) domains of R–Cu(111).

4. Conclusions

In summary, we investigated the reactivity and formation of Cu* nanoclusters on the (111) terraces of a stepped Cu surface by a combination of DFT and KMC simulations. DFT–computed adsorption energies of species relevant to a number of catalytic reactions revealed dramatically stronger (0.34 eV, on average) adsorbate–surface interactions for Cu* nanoclusters Cu_x/Cu(111), where $1 \leq x \leq 7$, compared to Cu(111). The unusual reactivity of Cu_x/Cu(111) was further confirmed by the stronger CO* binding (0.10 eV, on average) on Cu_x/Cu(111) than on Cu(211), a surface that is often employed as a model for undercoordinated nanoparticle sites. Our work highlighted that, under CO exposure, the ejection of Cu atoms from Cu(211) is thermodynamically and kinetically facilitated by adsorbate–adsorbate interactions in the step edges. Accordingly, we identified a BEP relationship based on which a CO* coverage change on Cu(211) from UHV (i.e., 0.00 ML) to 0.58 ML brings about remarkable reductions of 0.50 eV and 0.45 eV in the activation energy and energy of the ejection of a Cu atom from the step edge of Cu(211), respectively. By means of KMC simulation, we modeled CO* TPD spectra for desorption from Cu(111), Cu(211), and a roughened Cu(111) (R–Cu(111)) surface. In contrast to the pristine surfaces, R–Cu(111) exhibited two distinct peaks. The low temperature peak (162 K) was associated to CO* desorption from the "nanocluster–free" Cu(111) domains of the R–Cu(111) surface, while the high temperature peak (229 K) appeared at 10 K higher than the CO* desorption peak from Cu(211) step edges and corresponded to CO* desorption from the edges of the nanoclusters in the R–Cu(111) surface. We conclude that TPD holds promise for identifying roughened metal surfaces containing nanoclusters. Finally, our results showcase how surface

reaction (CO* desorption in this case) and surface restructuring can be combined in computational models. Such simulations can deal with the high complexity of heterogeneously catalyzed reactions and, in view of recent developments in KMC algorithms [84], could contribute to the accurate modeling of surface reactions at even larger scales that the ones presented herein.

Acknowledgment

The work was supported by the U.S. Department of Energy, Basic Energy Sciences (DOE-BES), Division of Chemical Sciences, Catalysis Science Program, grant DE-FG02-05ER15731. We used resources of the National Energy Research Scientific Computing Center (NERSC), a U.S. Department of Energy Office of Science User Facility located at Lawrence Berkeley National Laboratory, operated under Contract No. DE–AC02–05CH11231 using NERSC award BES-ERCAP0027367. We are also grateful for the computing resources and assistance of the UW–Madison Center by the High Throughput Computing (CHTC) in the Department of Computer Sciences. The CHTC is supported by UW–Madison, the Advanced Computing Initiative, the Wisconsin Alumni Research Foundation, the Wisconsin Institutes for Discovery, and the National Science Foundation, and is an active member of the OSG Consortium, which is supported by the National Science Foundation and the U.S. Department of Energy's Office of Science.

References

[1] Z.P. Jovanov, H.A. Hansen, A.S. Varela, P. Malacrida, A.A. Peterson, J.K. Nørskov, I.E.L. Stephens, I. Chorkendorff, Opportunities and challenges in the electrocatalysis of CO2 and CO reduction using bifunctional surfaces: A theoretical and experimental study of Au–Cd alloys, J. Catal. 343 (2016) 215–231. https://doi.org/10.1016/j.jcat.2016.04.008.

[2] G.A. Somorjai, M.A. Van Hove, Adsorbate-induced restructuring of surfaces, Prog. Surf. Sci. 30 (1989) 201–231. https://doi.org/10.1016/0079-6816(89)90009-9.

[3] R. Imbihl, G. Ertl, Oscillatory Kinetics in Heterogeneous Catalysis, Chem. Rev. 95 (1995) 697–733. https://doi.org/10.1021/cr00035a012.

[4] P. Fery, W. Moritz, D. Wolf, Structure determination of the (1×2) and (1×3) reconstructions of Pt(110) by low-energy electron diffraction, Phys. Rev. B. 38 (1988) 7275–7286. https://doi.org/10.1103/PhysRevB.38.7275.

[5] S. Zafeiratos, S. Piccinin, D. Teschner, Alloys in catalysis: Phase separation and surface segregation phenomena in response to the reactive environment, Catal. Sci. Technol. 2 (2012) 1787–1801. https://doi.org/10.1039/c2cy00487a.

[6] F. Tao, M.E. Grass, Y. Zhang, D.R. Butcher, J.R. Renzas, Z. Liu, J.Y. Chung, B.S. Mun, M. Salmeron, G.A. Somorjai, Reaction-Driven Restructuring of Rh-Pd and Pt-Pd Core-Shell Nanoparticles, Science (80-.). 322 (2008) 932–934. https://doi.org/10.1126/science.1164170.

[7] F. Gao, Y. Wang, D.W. Goodman, CO Oxidation over AuPd(100) from ultrahigh vacuum to near-atmospheric pressures: CO adsorption-induced surface segregation and reaction kinetics, J. Phys. Chem. C. 113 (2009) 14993–15000. https://doi.org/10.1021/jp9053132.

[8] K.I. Tanaka, T. Fujita, Y. Okawa, Oxygen induced order-disorder restructuring of a Cu(100) surface, Surf. Sci. 401 (1998). https://doi.org/10.1016/S0039-6028(97)01011-X.

[9] P. Thostrup, E. Kruse Vestergaard, T. An, E. Lægsgaard, F. Besenbacher, Co-induced restructuring of Pt(110)-(1×2): Bridging the pressure gap with high-pressure scanning tunneling microscopy, J. Chem. Phys. 118 (2003) 3724–3730. https://doi.org/10.1063/1.1540611.

[10] F. Yang, M.S. Chen, D.W. Goodman, Sintering of Au Particles Supported on TiO 2 (110)

during CO Oxidation, J. Phys. Chem. C. 113 (2009) 254–260. https://doi.org/10.1021/jp807865w.

[11] E. Kampshoff, N. Waelchli, A. Menck, K. Kern, Hydrogen-induced missing-row reconstructions of Pd(110) studied by scanning tunneling microscopy, Surf. Sci. 360 (1996) 55–60. https://doi.org/10.1016/0039-6028(96)00653-X.

[12] R. Cheula, M. Maestri, G. Mpourmpakis, Modeling Morphology and Catalytic Activity of Nanoparticle Ensembles under Reaction Conditions, ACS Catal. 10 (2020) 6149–6158. https://doi.org/10.1021/acscatal.0c01005.

[13] K.G. Papanikolaou, M.T. Darby, M. Stamatakis, Engineering the Surface Architecture of Highly Dilute Alloys: An ab Initio Monte Carlo Approach, ACS Catal. 10 (2020) 1224–1236. https://doi.org/10.1021/acscatal.9b04029.

[14] A.J. McCue, J.A. Anderson, CO induced surface segregation as a means of improving surface composition and enhancing performance of CuPd bimetallic catalysts, J. Catal. 329 (2015) 538–546. https://doi.org/10.1016/j.jcat.2015.06.002.

[15] B.W.J. Chen, L. Xu, M. Mavrikakis, Computational Methods in Heterogeneous Catalysis, Chem. Rev. 121 (2021) 1007–1048. https://doi.org/10.1021/acs.chemrev.0c01060.

[16] R. Bliem, J.E.S. Van Der Hoeven, J. Hulva, J. Pavelec, O. Gamba, P.E. De Jongh, M. Schmid, P. Blaha, U. Diebold, G.S. Parkinson, Dual role of CO in the stability of subnano Pt clusters at the Fe3 O4(001) surface, Proc. Natl. Acad. Sci. U. S. A. 113 (2016) 8921–8926. https://doi.org/10.1073/pnas.1605649113.

[17] M. Salmeron, B. Eren, High-Pressure Scanning Tunneling Microscopy, Chem. Rev. 121 (2021) 962–1006. https://doi.org/10.1021/acs.chemrev.0c00429.

[18] F. Tao, S. Dag, L.W. Wang, Z. Liu, D.R. Butcher, H. Bluhm, M. Salmeron, G.A. Somorjai, Break-up of stepped platinum catalyst surfaces by high co coverage, Science (80-.). 327 (2010) 850–853. https://doi.org/10.1126/science.1182122.

[19] B. Eren, D. Zherebetskyy, L.L. Patera, C.H. Wu, H. Bluhm, C. Africh, L.-W. Wang, G.A. Somorjai, M. Salmeron, Activation of Cu(111) surface by decomposition into nanoclusters driven by CO adsorption, Science (80-.). 351 (2016) 475–478. https://doi.org/10.1126/science.aad8868.

[20] B. Eren, M. Salmeron, Predicting Surface Clustering at Ambient Conditions from Thermodynamic Data, J. Phys. Chem. C. 123 (2019) 8171–8176. https://doi.org/10.1021/acs.jpcc.8b08287.

[21] J. Wang, M. McEntee, W. Tang, M. Neurock, A.P. Baddorf, P. Maksymovych, J.T. Yates, Formation, Migration, and Reactivity of Au-CO Complexes on Gold Surfaces, J. Am. Chem. Soc. 138 (2016) 1518–1526. https://doi.org/10.1021/jacs.5b09052.

[22] J. Hrbek, F.M. Hoffmann, J.B. Park, P. Liu, D. Stacchiola, Y.S. Hoo, S. Ma, A. Nambu,

J.A. Rodriguez, M.G. White, Adsorbate-driven morphological changes of a gold surface at low temperatures, J. Am. Chem. Soc. 130 (2008) 17272–17273. https://doi.org/10.1021/ja8081268.

[23] P. Cernota, K. Rider, H.A. Yoon, M. Salmeron, G. Somorjai, Dense structures formed by CO on Rh(111) studied by scanning tunneling microscopy, Surf. Sci. 445 (2000) 249–255. https://doi.org/10.1016/S0039-6028(99)01073-0.

[24] C.T. Campbell, B.E. Koel, K.A. Daube, Surface science studies of the water–gas shift reaction on a model Cu(111) catalyst, J. Vac. Sci. Technol. A Vacuum, Surfaces, Film. 5 (1987) 810–813. https://doi.org/10.1116/1.574354.

[25] P.B. Rasmussen, P.M. Holmblad, T. Askgaard, C. V. Ovesen, P. Stoltze, J.K. Nørskov, I. Chorkendorff, Methanol synthesis on Cu(100) from a binary gas mixture of CO2 and H2, Catal. Letters. 26 (1994) 373–381. https://doi.org/10.1007/BF00810611.

[26] M. Behrens, F. Studt, I. Kasatkin, S. Kühl, M. Hävecker, F. Abild-Pedersen, S. Zander, F. Girgsdies, P. Kurr, B. Kniep, M. Tovar, R.W. Fischer, J.K. Nørskov, R. Schlögl, The Active Site of Methanol Synthesis over Cu/ZnO/Al 2 O 3 Industrial Catalysts, Science (80-.). 336 (2012) 893–897. https://doi.org/10.1126/science.1219831.

[27] L.C. Grabow, M. Mavrikakis, Mechanism of methanol synthesis on cu through CO2 and CO hydrogenation, ACS Catal. 1 (2011) 365–384. https://doi.org/10.1021/cs200055d.

[28] S. Kandoi, A.A. Gokhale, L.C. Grabow, J.A. Dumesic, M. Mavrikakis, Why Au and Cu Are More Selective Than Pt for Preferential Oxidation of CO at Low Temperature, Catal. Letters. 93 (2004) 93–100. https://doi.org/10.1023/B:CATL.0000016955.66476.44.

[29] S. Yamamoto, K. Andersson, H. Bluhm, G. Ketteler, D.E. Starr, T. Schiros, H. Ogasawara, L.G.M. Pettersson, M. Salmeron, A. Nilsson, Hydroxyl-Induced Wetting of Metals by Water at Near-Ambient Conditions, J. Phys. Chem. C. 111 (2007) 7848–7850. https://doi.org/10.1021/jp0731654.

[30] L. Xu, K.G. Papanikolaou, B.A.J. Lechner, L. Je, G.A. Somorjai, M. Salmeron, M. Mavrikakis, Formation of active sites on transition metals through reaction-driven migration of surface atoms, Science (80-.). 380 (2023) 70–76. https://doi.org/10.1126/science.add0089.

[31] L. Xu, M. Mavrikakis, Adsorbate-Induced Adatom Formation on Lithium, Iron, Cobalt, Ruthenium, and Rhenium Surfaces, JACS Au. 3 (2023) 2216–2225. https://doi.org/10.1021/jacsau.3c00256.

[32] B. Eren, D. Zherebetskyy, Y. Hao, L.L. Patera, L.W. Wang, G.A. Somorjai, M. Salmeron, One-dimensional nanoclustering of the Cu(100) surface under CO gas in the mbar pressure range, Surf. Sci. 651 (2016) 210–214. https://doi.org/10.1016/j.susc.2016.04.016.

[33] M. Roiaz, L. Falivene, C. Rameshan, L. Cavallo, S.M. Kozlov, G. Rupprechter, Roughening of Copper (100) at Elevated CO Pressure: Cu Adatom and Cluster Formation

Enable CO Dissociation, J. Phys. Chem. C. 123 (2019) 8112–8121. https://doi.org/10.1021/acs.jpcc.8b07668.

[34] G. Rupprechter, Operando Surface Spectroscopy and Microscopy during Catalytic Reactions: From Clusters via Nanoparticles to Meso-Scale Aggregates, Small. 17 (2021) 2004289. https://doi.org/10.1002/smll.202004289.

[35] L.-Y. Gan, R.-Y. Tian, X.-B. Yang, H.-D. Lu, Y.-J. Zhao, Catalytic Reactivity of CuNi Alloys toward H 2 O and CO Dissociation for an Efficient Water–Gas Shift: A DFT Study, J. Phys. Chem. C. 116 (2012) 745–752. https://doi.org/10.1021/jp208119x.

[36] B. Eren, R.S. Weatherup, N. Liakakos, G.A. Somorjai, M. Salmeron, Dissociative Carbon Dioxide Adsorption and Morphological Changes on Cu(100) and Cu(111) at Ambient Pressures, J. Am. Chem. Soc. 138 (2016) 8207–8211. https://doi.org/10.1021/jacs.6b04039.

[37] B. Eren, Z. Liu, D. Stacchiola, G.A. Somorjai, M. Salmeron, Structural Changes of Cu(110) and Cu(110)-(2 × 1)-O Surfaces under Carbon Monoxide in the Torr Pressure Range Studied with Scanning Tunneling Microscopy and Infrared Reflection Absorption Spectroscopy, J. Phys. Chem. C. 120 (2016) 8227–8231. https://doi.org/10.1021/acs.jpcc.6b02143.

[38] G. Kresse, J. Furthmüller, Efficiency of ab-initio total energy calculations for metals and semiconductors using a plane-wave basis set, Comput. Mater. Sci. 6 (1996) 15–50. https://doi.org/10.1016/0927-0256(96)00008-0.

[39] G. Kresse, J. Hafner, Ab initio molecular dynamics for liquid metals, Phys. Rev. B. 47 (1993) 558–561. https://doi.org/10.1103/PhysRevB.47.558.

[40] P.E. Blöchl, Projector augmented-wave method, Phys. Rev. B. 50 (1994) 17953–17979. https://doi.org/10.1103/PhysRevB.50.17953.

[41] G. Kresse, A. Gil, P. Sautet, Significance of single-electron energies for the description of CO on Pt(111), Phys. Rev. B. 68 (2003) 073401. https://doi.org/10.1103/PhysRevB.68.073401.

[42] P.H.T. Philipsen, E. van Lenthe, J.G. Snijders, E.J. Baerends, Relativistic calculations on the adsorption of CO on the (111) surfaces of Ni, Pd, and Pt within the zeroth-order regular approximation, Phys. Rev. B. 56 (1997) 13556–13562. https://doi.org/10.1103/PhysRevB.56.13556.

[43] S.E. Mason, I. Grinberg, A.M. Rappe, First-principles extrapolation method for accurate CO adsorption energies on metal surfaces, Phys. Rev. B. 69 (2004) 161401. https://doi.org/10.1103/PhysRevB.69.161401.

[44] G. Pacchioni, C. Di Valentin, D. Dominguez-Ariza, F. Illas, T. Bredow, T. Klüner, V. Staemmler, Bonding of NH 3 , CO, and NO to NiO and Ni-doped MgO: a problem for density functional theory, J. Phys. Condens. Matter. 16 (2004) S2497–S2507.

https://doi.org/10.1088/0953-8984/16/26/024.

[45] J.P. Perdew, K. Burke, M. Ernzerhof, Generalized Gradient Approximation Made Simple, Phys. Rev. Lett. 77 (1996) 3865–3868. https://doi.org/10.1103/PhysRevLett.77.3865.

[46] M. Gajdoš, J. Hafner, CO adsorption on Cu(111) and Cu(001) surfaces: Improving site preference in DFT calculations, Surf. Sci. 590 (2005) 117–126. https://doi.org/10.1016/j.susc.2005.04.047.

[47] S. Vollmer, G. Witte, C. Wöll, Determination of site specific adsorption energies of CO on copper, Catal. Letters. 77 (2001) 97–101. https://doi.org/10.1023/A:1012755616064.

[48] P. Hollins, J. Pritchard, Interactions of CO molecules adsorbed on Cu(111), Surf. Sci. 89 (1979) 486–495. https://doi.org/10.1016/0039-6028(79)90633-2.

[49] W.P. Davey, Precision Measurements of the Lattice Constants of Twelve Common Metals, Phys. Rev. 25 (1925) 753–761. https://doi.org/10.1103/PhysRev.25.753.

[50] H.J. Monkhorst, J.D. Pack, Special points for Brillouin-zone integrations, Phys. Rev. B. 13 (1976) 5188–5192. https://doi.org/10.1103/PhysRevB.13.5188.

[51] G. Henkelman, B.P. Uberuaga, H. Jónsson, Climbing image nudged elastic band method for finding saddle points and minimum energy paths, J. Chem. Phys. 113 (2000) 9901–9904. https://doi.org/10.1063/1.1329672.

[52] G. Henkelman, H. Jónsson, A dimer method for finding saddle points on high dimensional potential surfaces using only first derivatives, J. Chem. Phys. 111 (1999) 7010–7022. https://doi.org/10.1063/1.480097.

[53] M. Stamatakis, D.G. Vlachos, A graph-theoretical kinetic Monte Carlo framework for on-lattice chemical kinetics, J. Chem. Phys. 134 (2011) 214115. https://doi.org/10.1063/1.3596751.

[54] M. Stamatakis, Kinetic modelling of heterogeneous catalytic systems, J. Phys. Condens. Matter. 27 (2015). https://doi.org/10.1088/0953-8984/27/1/013001.

[55] M. Stamatakis, Zacros: Advanced Lattice-KMC Simulation Made Easy, (2013). https://zacros.org/.

[56] J. Nielsen, M. D'Avezac, J. Hetherington, M. Stamatakis, Parallel kinetic Monte Carlo simulation framework incorporating accurate models of adsorbate lateral interactions, J. Chem. Phys. 139 (2013) 224706. https://doi.org/10.1063/1.4840395.

[57] M. Pineda, M. Stamatakis, Kinetic Monte Carlo simulations for heterogeneous catalysis: Fundamentals, current status and challenges, J. Chem. Phys. 073101 (2022). https://doi.org/10.1063/5.0083251.

[58] K.G. Papanikolaou, M. Stamatakis, Toward the accurate modeling of the kinetics of

surface reactions using the kinetic Monte Carlo method, in: Front. Nanosci., 2020: pp. 95–125. https://doi.org/10.1016/B978-0-12-821495-4.00007-5.

[59] K.G. Papanikolaou, M.T. Darby, M. Stamatakis, Engineering the Surface Architecture of Highly Dilute Alloys: An ab Initio Monte Carlo Approach, ACS Catal. 10 (2020) 1224–1236. https://doi.org/10.1021/acscatal.9b04029.

[60] C. Wu, D.J. Schmidt, C. Wolverton, W.F. Schneider, Accurate coverage-dependence incorporated into first-principles kinetic models: Catalytic NO oxidation on Pt (111), J. Catal. 286 (2012) 88–94. https://doi.org/10.1016/j.jcat.2011.10.020.

[61] M.G. Evans, M. Polanyi, Inertia and driving force of chemical reactions, Trans. Faraday Soc. 34 (1938) 11. https://doi.org/10.1039/tf9383400011.

[62] S. Matera, W.F. Schneider, A. Heyden, A. Savara, Progress in Accurate Chemical Kinetic Modeling, Simulations, and Parameter Estimation for Heterogeneous Catalysis, ACS Catal. 9 (2019) 6624–6647. https://doi.org/10.1021/acscatal.9b01234.

[63] C. Wu, D.J. Schmidt, C. Wolverton, W.F. Schneider, Accurate coverage-dependence incorporated into first-principles kinetic models: Catalytic NO oxidation on Pt (111), J. Catal. 286 (2012) 88–94. https://doi.org/10.1016/j.jcat.2011.10.020.

[64] L. Xu, J. Lin, Y. Bai, M. Mavrikakis, Atomic and Molecular Adsorption on Cu(111), Top. Catal. 61 (2018) 736–750. https://doi.org/10.1007/s11244-018-0943-0.

[65] G. Blyholder, Molecular Orbital View of Chemisorbed Carbon Monoxide, J. Phys. Chem. 68 (1964) 2772–2777. https://doi.org/10.1021/j100792a006.

[66] E.R.A. Beronio, A.N.P. Hipolito, J.D. Ocon, H. Nakanishi, H. Kasai, A.A.B. Padama, Cluster size effects on the adsorption of CO, O, and CO 2 and the dissociation of CO 2 on two-dimensional Cu x (x = 1, 3, and 7) clusters supported on Cu(111) surface: a density functional theory study, J. Phys. Condens. Matter. 32 (2020) 405201. https://doi.org/10.1088/1361-648X/ab945d.

[67] J.-F. Paul, J. Pérez-Ramírez, F. Ample, J.M. Ricart, Theoretical Studies of N 2 O Adsorption and Reactivity to N 2 and NO on Rh(111), J. Phys. Chem. B. 108 (2004) 17921–17927. https://doi.org/10.1021/jp048138h.

[68] K.G. Papanikolaou, M. Stamatakis, The catalytic decomposition of nitrous oxide and the NO + CO reaction over Ni/Cu dilute and single atom alloy surfaces: first-principles microkinetic modelling, Catal. Sci. Technol. 11 (2021) 3681–3696. https://doi.org/10.1039/D1CY00011J.

[69] A. Bogicevic, K.C. Hass, NO pairing and transformation to N2O on Cu(1 1 1) and Pt(1 1 1) from first principles, Surf. Sci. 506 (2002). https://doi.org/10.1016/S0039-6028(02)01491-7.

[70] M. Gajdoš, A. Eichler, J. Hafner, G. Meyer, K.H. Rieder, CO adsorption on a Cu(211)

surface: First-principle calculation and STM study, Phys. Rev. B - Condens. Matter Mater. Phys. 71 (2005) 1–7. https://doi.org/10.1103/PhysRevB.71.035402.

[71] W. Kirstein, B. Krüger, F. Thieme, CO adsorption studies on pure and Ni-covered Cu(111) surfaces, Surf. Sci. 176 (1986) 505–529. https://doi.org/10.1016/0039-6028(86)90052-X.

[72] J. Pritchard, On the structure of CO adlayers on Cu(100) and Cu(111), Surf. Sci. 79 (1979) 231–244. https://doi.org/10.1016/0039-6028(79)90039-6.

[73] R. Raval, S.F. Parker, M.E. Pemble, P. Hollins, J. Pritchard, M.A. Chesters, FT-rairs, eels and leed studies of the adsorption of carbon monoxide on Cu(111), Surf. Sci. 203 (1988) 353–377. https://doi.org/10.1016/0039-6028(88)90088-X.

[74] Z. Lyu, S. Zhu, L. Xu, Z. Chen, Y. Zhang, M. Xie, T. Li, S. Zhou, J. Liu, M. Chi, M. Shao, M. Mavrikakis, Y. Xia, Kinetically Controlled Synthesis of Pd-Cu Janus Nanocrystals with Enriched Surface Structures and Enhanced Catalytic Activities toward CO2Reduction, J. Am. Chem. Soc. 143 (2021) 149–162. https://doi.org/10.1021/jacs.0c05408.

[75] A. Michaelides, Z.P. Liu, C.J. Zhang, A. Alavi, D.A. King, P. Hu, Identification of general linear relationships between activation energies and enthalpy changes for dissociation reactions at surfaces, J. Am. Chem. Soc. 125 (2003) 3704–3705. https://doi.org/10.1021/ja027366r.

[76] J.K. Nørskov, T. Bligaard, A. Logadottir, S. Bahn, L.B. Hansen, M. Bollinger, H. Bengaard, B. Hammer, Z. Sljivancanin, M. Mavrikakis, Y. Xu, S. Dahl, C.J.H. Jacobsen, Universality in Heterogeneous Catalysis, J. Catal. 209 (2002) 275–278. https://doi.org/10.1006/jcat.2002.3615.

[77] A.U. Nilekar, J. Greeley, M. Mavrikakis, A simple rule of thumb for diffusion on transition-metal surfaces, Angew. Chemie - Int. Ed. 45 (2006) 7046–7049. https://doi.org/10.1002/anie.200602223.

[78] L.T. Roling, M. Mavrikakis, Toward rational nanoparticle synthesis: Predicting surface intermixing in bimetallic alloy nanocatalysts, Nanoscale. 9 (2017) 15005–15017. https://doi.org/10.1039/c7nr04779g.

[79] L. Hansen, P. Stoltze, K.W. Jacobsen, J.K. Nørskov, Self-diffusion on copper surfaces, Phys. Rev. B. 44 (1991) 6523–6526. https://doi.org/10.1103/PhysRevB.44.6523.

[80] K.G. Papanikolaou, Y. Shi, R. Schimmenti, Y. Xia, M. Mavrikakis, The role of coverage effects on the structure–sensitivity of formic acid electrooxidation on Pd surfaces, J. Catal. 417 (2023) 408–420. https://doi.org/10.1016/j.jcat.2022.12.025.

[81] M. Stamatakis, S. Piccinin, Rationalizing the Relation between Adlayer Structure and Observed Kinetics in Catalysis, ACS Catal. 6 (2016) 2105–2111. https://doi.org/10.1021/acscatal.5b02876.

[82] K.G. Papanikolaou, M. Stamatakis, Toward the accurate modeling of the kinetics of surface reactions using the kinetic Monte Carlo method, in: Comput. Model. Nanomater., 2020: pp. 95–125. https://doi.org/10.1016/B978-0-12-821495-4.00007-5.

[83] S.L. Tait, Z. Dohnálek, C.T. Campbell, B.D. Kay, n -alkanes on MgO(100). I. Coverage-dependent desorption kinetics of n-butane, J. Chem. Phys. 122 (2005). https://doi.org/10.1063/1.1883629.

[84] S. Ravipati, G.D. Savva, I.-A. Christidi, R. Guichard, J. Nielsen, R. Réocreux, M. Stamatakis, Coupling the time-warp algorithm with the graph-theoretical kinetic Monte Carlo framework for distributed simulations of heterogeneous catalysts, Comput. Phys. Commun. 270 (2022) 108148. https://doi.org/10.1016/j.cpc.2021.108148.